Progress in Natural Science: Materials International 32 (2022) 415–423

HOSTED BY

Contents lists available at ScienceDirect

Progress in Natural Science: Materials International

journal homepage: www.elsevier.com/locate/pnsmi

Influence of parameters on the microstructure of a duplex stainless steel joint welded by a GMAW welding process

Sandra Chacón-Fernández *, Antonio Portolés García, Gerardo Romaní Labanda

Universidad Politécnica de Madrid, Escuela Técnica Superior de Ingenieros Industriales, UPM, c/ José Gutiérrez Abascal, 2, 28006, Madrid, Spain

ARTICLE INFO

Keywords:
Welding
Heat input
GMAW
Duplex stainless steels (DSS)
Finite element model (FEM)

ABSTRACT

Duplex stainless steels (DSSs) are widely used in industry for their desirable properties. Any fusion welding technique modifies the microstructure and, consequently, the properties of the material. This paper presents a parametric study of the variables that determine the energy contribution (current, voltage and welding speed) and the structural modifications produced during gas metal arc welding. The analysis comprises metallographic study, phase balance, dimensioning of the weld beads and tensile and hardness tests. The influence of the variables studied on the thermal cycles obtained (temperatures reached and cooling rate) was determined by using a finite element model. The results showed that, in addition to the indicated parameters, the parameter power transfer per volume (W/m^3) and the geometry in the bead must be controlled due to their influence on the heat flow distribution and phase balance.

1. Introduction

Duplex stainless steels (DSSs) are iron–chromium–nickel alloys that also contain other elements such as carbon (up to 0.03 wt %). DSSs contain two phases in their structure: ferrite and austenite. The ferrite/austenite (α/γ) ratio can reach up to 70/30 [1,2]. Physical, mechanical and chemical properties are influenced by composition and thermal history; these factors determine the microstructure and the percentage of each phase that appears in the material. The main chemical elements that make up stainless steels are chromium, nickel, molybdenum, nitrogen, carbon, manganese, niobium, titanium, copper, silicon and tungsten [3]. Sulphur and phosphorus impurities are also present. There are five types of DSSs, classified according to their chromium content: low-alloy duplexes, standard duplexes, duplexes with 25% chromium, super-duplexes and hyper-duplexes. Each of these has a different resistance to corrosion, so they are used in different fields, ranging from the food industry to the petrochemical or automobile industries [4]. Specifically, DSS UNS S32205 is considered an advanced material owing to its corrosion resistance. For this reason, its main applications are in the chemical, petrochemical, paper and mining industries; storage tanks and piping systems; desalination and effluent treatment plants; heat exchangers; and containers and piping systems in ships and civil works [5–9].

The phase balance determines the properties of DSSs. Fusion welding processes modify the thermal history of the material and, consequently, the α/γ balance. For this reason, discrete zones are created in a weld joint, namely a bead, a heat affected zone (HAZ) and the base metal (BM). The bead corresponds to a melted area wherein the chemical composition of the BM, filler metal and shielding gas influence the microstructure. In the HAZ, the microstructure formed is dependent on the rate of cooling from the maximum temperature to the end-of-transformation temperature. In welded joints, it is important to study the heat input, the evolution of the temperature and the cooling rate [10–14]. When cooling is very rapid, there is not enough time for sufficient austenite to form in the molten zone or in the HAZ, resulting in a loss of optimum phase balance [15].

Gas metal arc welding (GMAW) is a gas-shielded electric arc welding process. The necessary heat is generated by an arc established between a consumable electrode and the metal to be welded. The consumable electrode is a solid wire, which is continuously fed and transferred as droplets through the arc into the molten pool, where it becomes the deposited metal. This process that is highly oriented to industrial production due to the high rate of metal deposition [16–18]. It is commonly used in robotic welding.

The parameter that significantly influences the phase balance and the properties of the welded joint is the thermal cycle to which the material is subjected, which is dependent on the energy or heat supplied during welding. The energy provided (heat input) in electric arc welding processes (expressed in kJ/mm), is given by the formula:

* Corresponding author.
E-mail addresses: sandra.chacon@upm.es (S. Chacón-Fernández), antonio.portoles@upm.es (A. Portolés García), gerardo.romani@upm.es (G. Romaní Labanda).

https://doi.org/10.1016/j.pnsc.2022.06.003
Received 1 February 2022; Received in revised form 6 May 2022; Accepted 22 June 2022
Available online 2 July 2022

Table 1
Chemical composition of DSS UNS S32205 (wt. %).

Material	C	Mn	Si	P	S	Cr	Ni	Mo	N
S32205	0.014	1.41	0.44	0.030	0.003	22.3	5.09	3.33	0.18

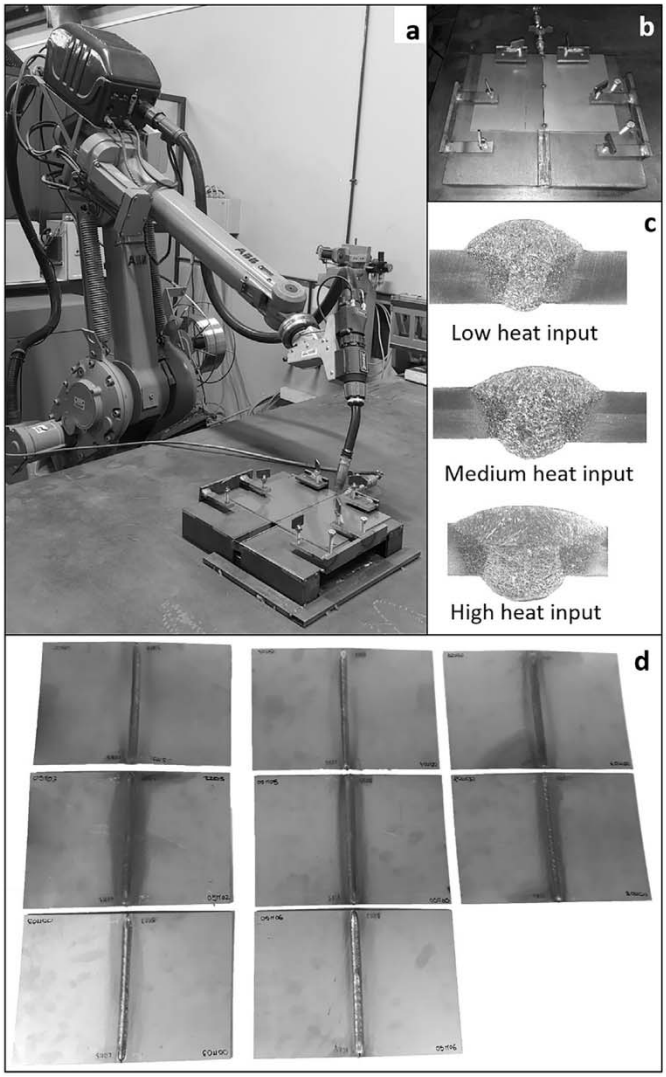

Fig. 1. (a) An image of the welding robot. (b) Details of the anchoring system of the pieces during welding with the backing gas. (c) Macrographs of the coupons made with low, medium and high heat inputs. (d) Welding coupons.

Table 2
GMAW parameters for DSS UNS S32205.

Coupon	Welding speed (mm/s)	Wire feed speed (m/min)	Current (A)	Voltage (V)	Heat input (kJ/mm)
1	3.5	2.75	98	18.4	0.412
2	3.2	2.75	96	18.5	0.444
3	4	2.75	98	18.55	0.364
4	3.5	2.4	82	16.65	0.312
5	3.5	3	102	18.25	0.425
6	3.5	2.75	100	16.15	0.369
7	3.5	2.75	102	19.25	0.449
8	3.5	2.25	76	15.5	0.269

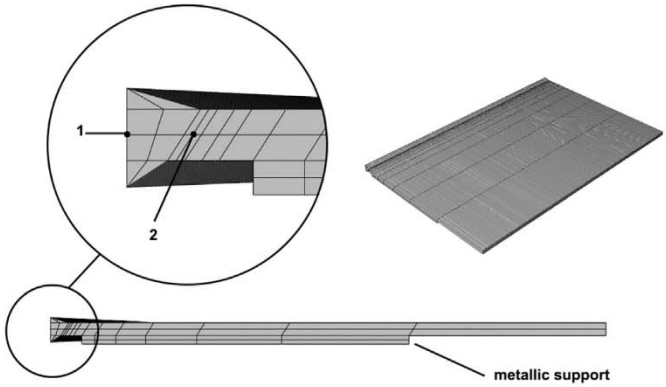

Fig. 2. Mesh used for the finite element model.

Table 3
Dimensions of all welds.

Coupon	Root dimensions (mm)		Face dimensions (mm)	
	Width	Excess penetration	Width	Excess weld metal
1	4.78	1.56	8.62	1.23
2	5.45	1.91	9.11	0.97
3	4.43	1.23	7.85	1.39
4	3	0.94	7.25	1.8
5	4.8	1.6	9.15	1.32
6	5.43	1.96	7.69	1.17
7	4.99	1.41	8.86	1.09
8	2.47	0.43	7.01	1.78

$$H = \rho \frac{UI}{v} 10^{-3} \quad (1)$$

where U is the voltage (in V), I is the current (in A), v is the welding speed (in mm/s) and ρ is the process performance parameter (0.8 for GMAW, as per UNE-EN 10111) [19,20].

This article analyses the influence of the current, voltage and welding speed, individually and together as heat input, on the microstructure of the weld bead and HAZ during robotic GMAW, and their influence on the properties of the welded joints. The microstructure was studied by optical microscopy. The influence of the different parameters on thermal cycles was studied using a finite element model [14,21]. Mechanical characterisation was performed via tensile testing and hardness chains.

2. Materials and methods

2.1. Materials

DSS UNS S32205, with dimensions of 200 × 150 × 3 mm without a bevel, was used as the BM. DSS ER2209 wire with a composition similar to UNS S32205 and a diameter of 1.2 mm was used as a filler metal. The chemical composition of the UNS S32205 duplex was determined by emission spectroscopy, using AQE15010-SPECTROLAB equipment. The laboratory confirmed that the sample chemically matched a S31803/S32205-type DSS. Table 1 shows the chemical composition of the material used. The mechanical properties measured for the as-received material were 803 N/mm^2 for tensile strength and a hardness of 259 HV. The BM presents an oriented microstructure formed due to the deformation process.

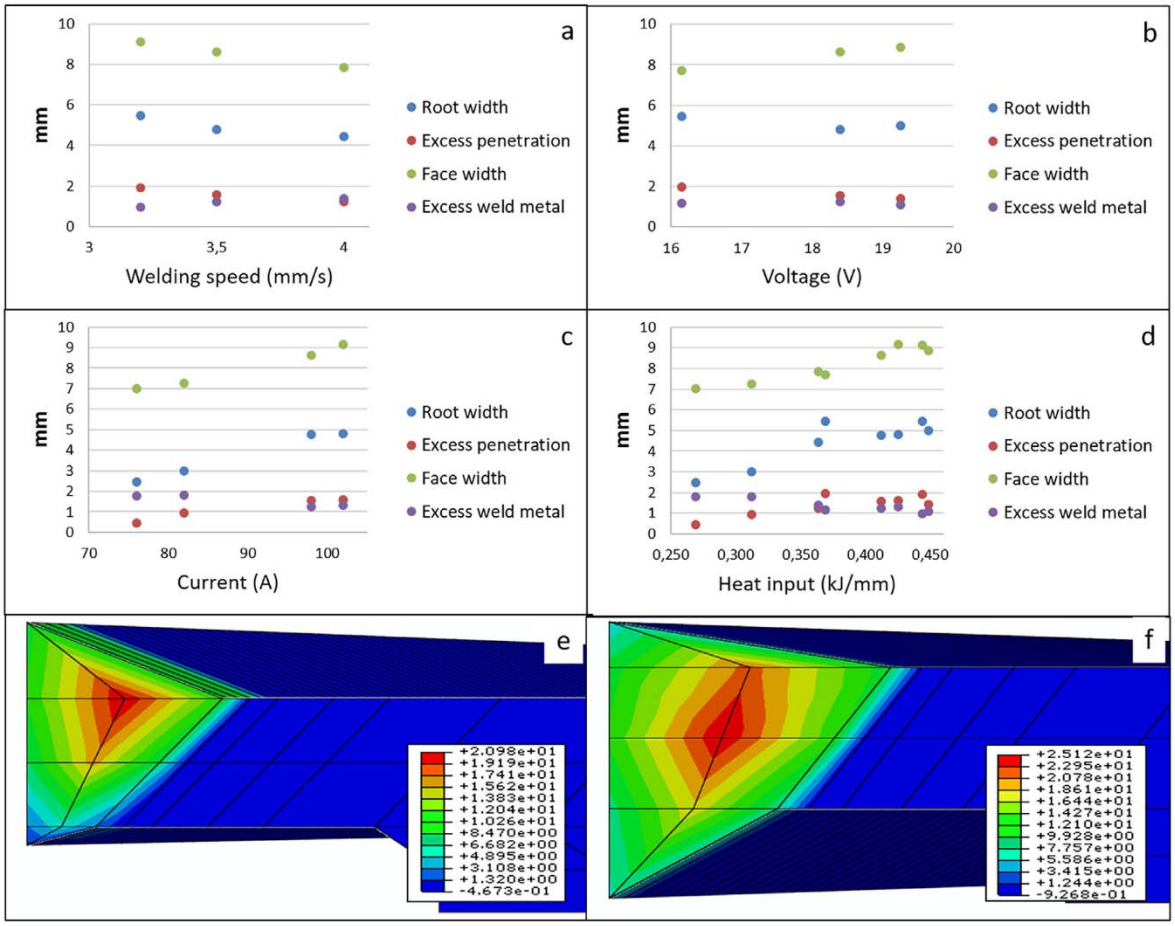

Fig. 3. Influence of parameters on the dimensions of the welded area: (a) welding speed, (b) voltage, (c) current, and (d) heat input. (e and f) Influence of geometry on heat flow (W/m^2).

2.2. Methods

2.2.1. Welding

GMAW was carried out with an IR1400 ABB robot using a pulsed arc. Two sheets were joined, leaving a 1.5 mm gap, as shown in Fig. 1a and b. A thickness of 3 mm was used, because this allows welding to be carried out in a single pass and without bevelling the edges; in this way, the welding speed, current and voltage can be analysed individually. An anchoring system for the weld coupons was designed in which backing gas was injected to protect the root of the weld. The shielding gas used was a mixture of argon with 2% CO_2, with a flow rate of 14 L/min in the zone of the bead face and 1 L/min in the root (backing gas). Fig. 1b shows the details of the system used for anchoring the coupons and the gas supplier.

The welds were made in a single pass. The influence of the following parameters was studied: welding speed, wire feed speed and voltage. Table 2 shows the matrix of experiments, as well as the actual values of current and voltage used during welding. A wider variation in the parameters was not tested in order to avoid causing defects that may compromise the results.

Fig. 1d shows the welding coupons made in this work. Coupon 8 was made with a low heat input, coupon 3 was made with a medium heat input and coupon 7 was made with a high heat input. Fig. 1c shows macrographs of the three samples corresponding to low, medium and high heat inputs. The literature indicates that for thicknesses between 3.5 and 6 mm, with a gap between 3 and 4 mm and a single pass, the recommended heat input is between 0.4 and 0.8 kJ/mm [22]. In this case, the values were lower, a necessity due to the reduced thickness of the material.

2.2.2. Microstructural characterisation, phase balance and grain size

For the metallographic study, samples were extracted from a representative area, following the recommendations of standard UNE-EN ISO 15614-1:2018 [23]. To facilitate the handling and preparation of these samples, they were hot-embedded with methyl methacrylate resin. They were then sanded with water-based sandpaper of different grits, ranging from 240 to 4000 grit. Then, they were polished with a 1 μm monocrystalline diamond suspension. Finally, chemical attack was carried out on the polished surface by immersion for 30 s in Beraha I reagent (20 mL HCl, 100 mL H_2O, 1 g $K_2S_2O_5$ and 2.4 g NH_4FHF) [24,25]. This reagent was used because it colours the phases for clearer identification and quantification under the metallographic microscope. Using image analysis software [26], the phase balance was obtained in a cross-section of the weld bead in each coupon. Six measurements were made in each zone (bead, HAZ and BM) to ensure the reliability of the measurement. Standard UNE-EN ISO 643:2020 [27] was followed to determine the grain size. The images were processed with specific software [28] using the Heyn method.

2.2.3. Weld dimensions, Vickers hardness and tensile testing

Regarding the dimensions of the bead, this study focussed on excess weld metal and excess penetration. A Nikon V-12A profile projector and the Digital Readout Counter Nikon SC-112 were used for the measurements. Standard UNE-EN ISO 5817:2014 [29] was followed to determine the optimal welds, considering excess weld metal and excess penetration without sagging.

Standard UNE-EN ISO 6507-1:2018 [30] was followed to measure hardness. Measurements were made using Leco M – 400 equipment. Tests were carried out in the form of a hardness line (chain of hardness)

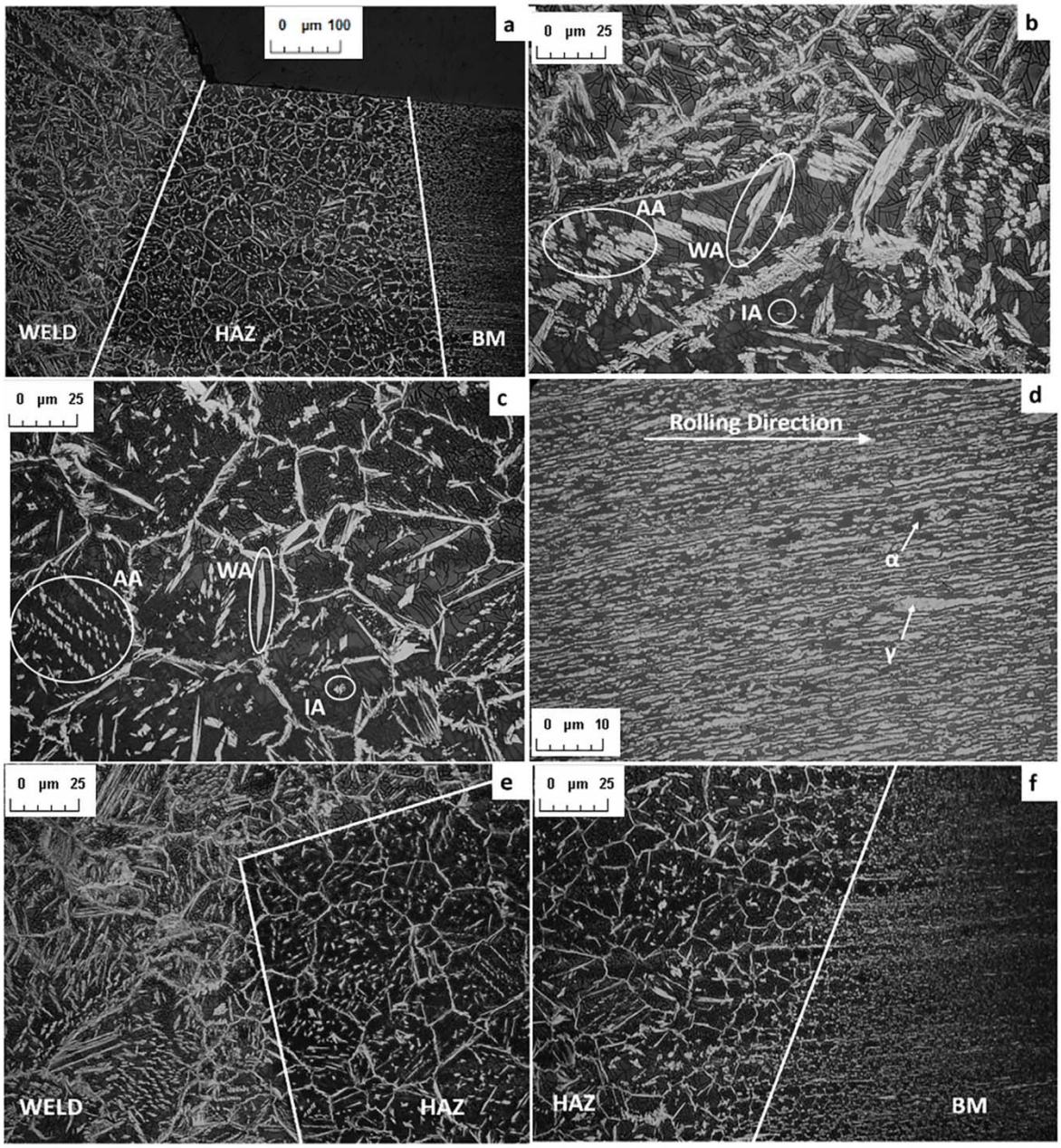

Fig. 4. The microstructure of weld coupon 7. (a) The three microstructure types: the weld bead, the HAZ and the BM. (b) The weld bead. (c) The HAZ. (d) The BM. (e) The bead–HAZ interface. (f) The HAZ–BM interface.

Table 4
Example of measurements made for the phase balance in coupon 3 with Cronbach's alpha reliability.

Coupon	Zone	% Ferrite						Average% ferrite	Cronbach's alpha
		F1	F2	F3	F4	F5	F6		
3	**Bead**	60.96	61.11	62.57	63.92	64.41	68.22	63.53	0.9546
	HAZ	80.36	80.62	80.97	82.16	82.37	82.51	81.50	0.9978

at an ambient temperature of approximately 25 °C via the Vickers method, with a load of 1 kg and a penetration time of 30 s. The hardness line was made 1 mm from the surface of the bead. Hardness was measured in the bead, the HAZ and the BM; three prints were made in each zone.

Tensile tests were carried out according to standard UNE-EN ISO 6892-1:2017 [31] at an ambient temperature of approximately 25 °C. Excess weld metal in the bead and excess penetration were removed by milling. Tests were carried out using MTS 810 equipment.

2.2.4. Finite element modelling

The Abaqus software [32] was used to realise and validate the finite element model, following the protocols published in our previous work [33–35]. The thermal model allows determining the thermal cycles that

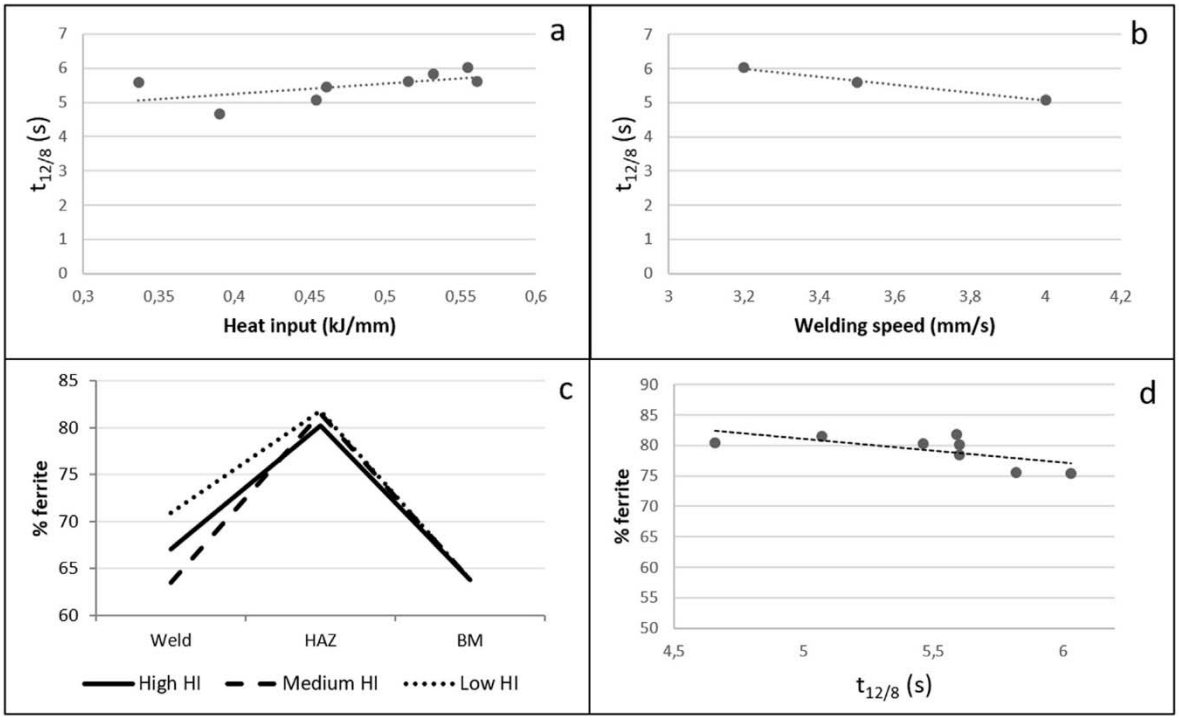

Fig. 5. (a) Heat input (HI) vs $t_{12/8}$, (b) welding speed vs $t_{12/8}$, (c) % ferrite dependence on the weld area vs heat input and (d) % ferrite vs $t_{12/8}$ in the HAZ.

the material undergoes due to heat input. The variation in properties with temperature was taken into account while constructing the model [36,37]. The properties of the materials used to make the thermal model were density, thermal conductivity, latent heat of fusion and specific heat. The initial temperature was considered to be room temperature (20 °C). The model considers heat transfer by conduction through the material and by convection and radiation through the outer surfaces. The model considers the real size of the bead, contemplating its elements as the heat input generators. In this way, the temperature distribution is obtained at each instant of time in each node. This approach allows calculating the size of the HAZ and the thermal cycles, both in the bead and in the HAZ.

The most common and widely accepted considerations in the field were used to realise the thermal model [15,38,39]. Because it is a symmetrical model (from the point of view of geometry and heat input) with respect to the axis of the bead, this allows modelling half of the geometry, simplifying the calculations. The austenitic stainless steel support on which the welding coupon is supported was also considered in the model.

Fig. 2 shows the mesh used for the finite element simulation, indicating the most representative points for the present study. Point 1, located in the central zone of the weld bead, was chosen as the representative node of said zone. Point 2, located 0.5 mm away from the bead–HAZ interface, was chosen as representative of the HAZ. Points 1 and 2 were used for the subsequent calculations.

3. Results and discussion

3.1. Weld dimensions

Table 3 shows the results obtained after measuring the height and width of the bead face and root. The equipment used allows a resolution of 1 μm. The values were rounded to the nearest 0.01 mm.

Fig. 3 shows the influence of the different parameters on the bead dimensions. The influence of welding speed in shown in Fig. 3a: as the welding speed increases, the excess weld metal also increases because there is not enough time for the BM to melt. For the same reason, the width of the face, the width of the root and the excess penetration also decrease. Fig. 3b shows the influence of voltage on bead dimensions: as the voltage increases, the arc length increases. The filler metal falls from a greater height, favouring an increase in the width of the face area, reducing excess penetration. Very similar behaviour can be observed under the influence of current (Fig. 3c) and heat input (Fig. 3d). Increasing current leads to an increase in the amount of metal supplied. This generates an increase in heat in the area; thus, the width of the bead increases. This phenomenon also promotes excess penetration and width in the root zone. By promoting the penetration of molten metal towards the root, the excess weld metal is decreased.

Finite element modelling indicates that bead geometry modifies the manner in which heat is distributed to the BM. A higher excess weld metal promotes a higher heat flow in the bead face area (Fig. 3e), while reducing the excess weld metal promotes a more uniform heat distribution throughout the thickness (Fig. 3f). Modification of the heat flow towards the BM induces changes in the thermal cycles of the joint; thus, both the phase balance and the properties of the welded joint may be modified. It must be considered that a greater heat flow implies greater heat dissipation and, consequently, a faster cooling speed.

3.2. Microstructural characterisation

Fig. 4 shows the microstructure obtained in solder coupon 7. The dark area corresponds to ferrite and the light area corresponds to austenite. Fig. 4a shows the three types of microstructures obtained in each zone: the weld bead, the HAZ and the BM. The different observed austenitic morphologies for the bead (Fig. 4b) and the HAZ (Fig. 4c) are also shown.

In the bead (Fig. 4b), the austenite is fundamentally in the form of needles with distinct morphologies. When the needles are thin and elongated, they are known as Widmanstätten austenite (WA); when they are more irregular and wider, they are known as allotropic austenite (AA). Intragranular austenite (IA) is also observed, a structure characteristic of cast parts and whose proportion varies depending on the maximum temperature reached and the cooling rate [15].

In the HAZ (Fig. 4c), recrystallisation and an increase in grain size are observed due to the high temperatures reached. Consequently, a cellular grain morphology is clearly observed in the austenite surrounding the

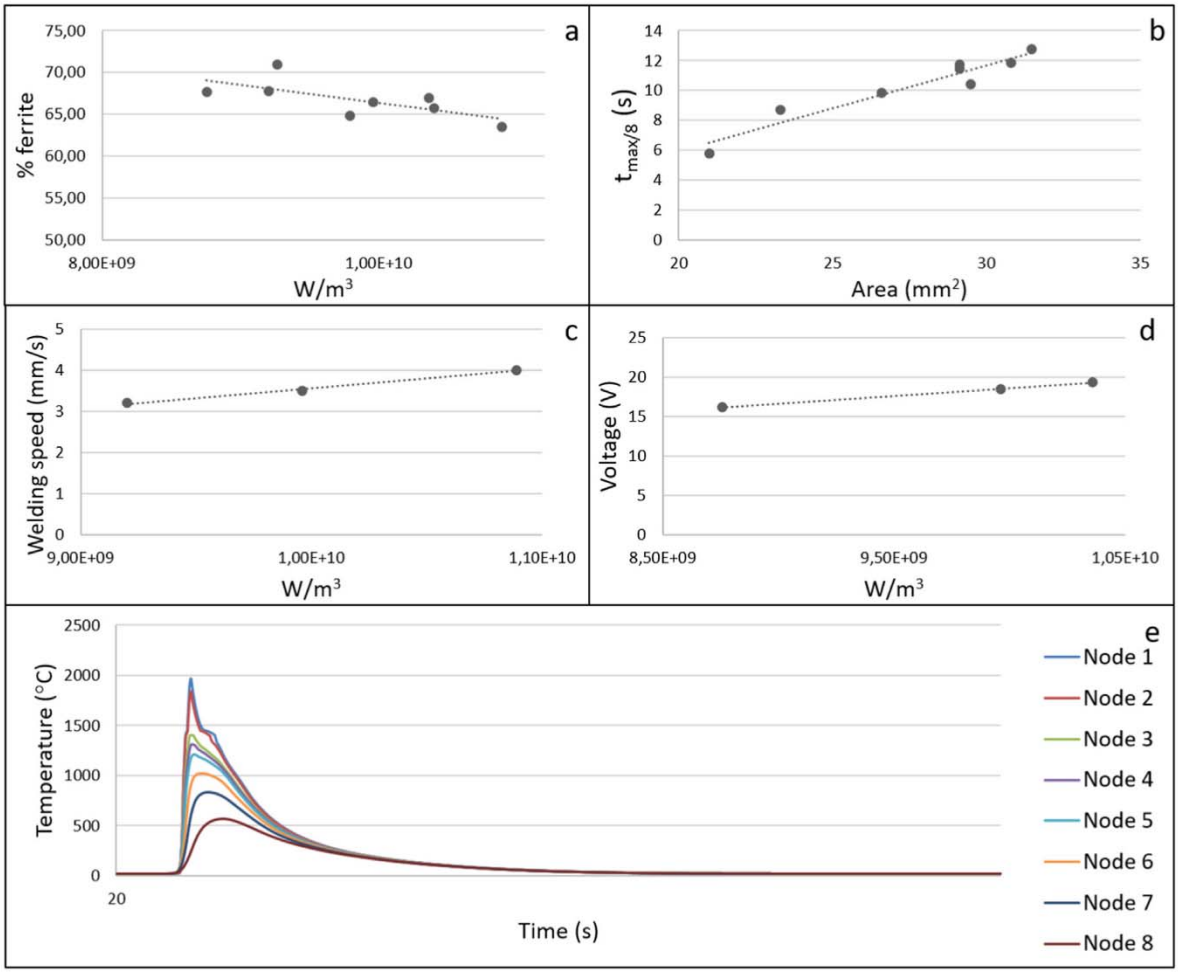

Fig. 6. (a) Percentage of ferrite obtained in the weld bead versus W/m^3 and (b) $t_{max/8}$ versus the weld bead area. (c) Relationship between welding speed and W/m^3 and (d) between voltage and W/m^3. (e) Examples of thermal cycles experienced by the nodes.

ferrite grains. This morphology is preferable, because austenite is tougher than ferrite and prevents any cracks formed in the ferrite zone from propagating to other grains. The grain size in this zone could increase up to G = 1 for the highest heat input values.

The proportions of WA and AA are significantly higher in the bead than in the HAZ. This is due to the fact that the melting temperature is exceeded in the bead and the cooling rate is faster than in the HAZ. The proportion of IA is higher in the HAZ, as it essentially corresponds to secondary austenite. This is because the melting temperature is not exceeded [15]. When comparing Fig. 4b and c, there is a difference between the bead and the HAZ in terms of the amount of ferrite.

In Fig. 4d, the BM appears as an oriented structure in the direction of lamination. This is a lamellar structure of austenite and ferrite.

The transition zones between the weld bead and the HAZ (Fig. 4e) and between the HAZ and the BM (Fig. 4f) are also shown. These structural modifications are characteristic of fusion welding processes. An increase in heat input causes both the HAZ and grain size to increase.

3.3. Phase balance and finite element modelling

To calculate the phase balance, six measurements were taken in the bead and the HAZ in each section, and the arithmetic mean was calculated. To increase reliability, statistical analysis was conducted by using Cronbach's alpha reliability analysis [40], which measures reliability on a scale of 0–1:

$$\alpha = \frac{K}{K-1}\left[1 - \frac{\sum Vi}{Vt}\right] \quad (2)$$

where K is the number of elements, Vi the variance of each element and Vt the total variance. As an example, Table 4 shows the result obtained for measurements of the bead and the HAZ corresponding to coupon 3 (presented as the average of six measurements for each zone).

The finite element model shows that the influence of the welding parameters is different depending on the area considered (the bead or the HAZ). The parametric study was carried out at points 1 and 2 (indicated in Fig. 2) to obtain comparable results. Point 1 is always in the central area of the bead and point 2 is 0.5 mm from the bead–HAZ interface.

The finite element model allowed determining the residence time in the temperature range between 1200 and 800 °C ($t_{12/8}$) for the HAZ. This parameter is particularly important because ferrite transforms into austenite in this temperature range. For the formation of austenite to be stable, this time must be equal to or greater than 10 s [14]. The finite element model revealed that the heat input influences $t_{12/8}$. Low heat input implies a low $t_{12/8}$; consequently, the cooling rate is faster, and so the proportion of austenite would be lower and the proportion of ferrite would be higher. Conversely, a larger heat input results in a larger $t_{12/8}$. Hence, the proportion of austenite would be higher (Fig. 5a and d). The parameter that most influences $t_{12/8}$ is the welding speed, as conduction promotes heat dissipation towards the HAZ. For this reason, the HAZ increases in size, resulting in slower cooling rates (Fig. 5b). Fig. 5c shows

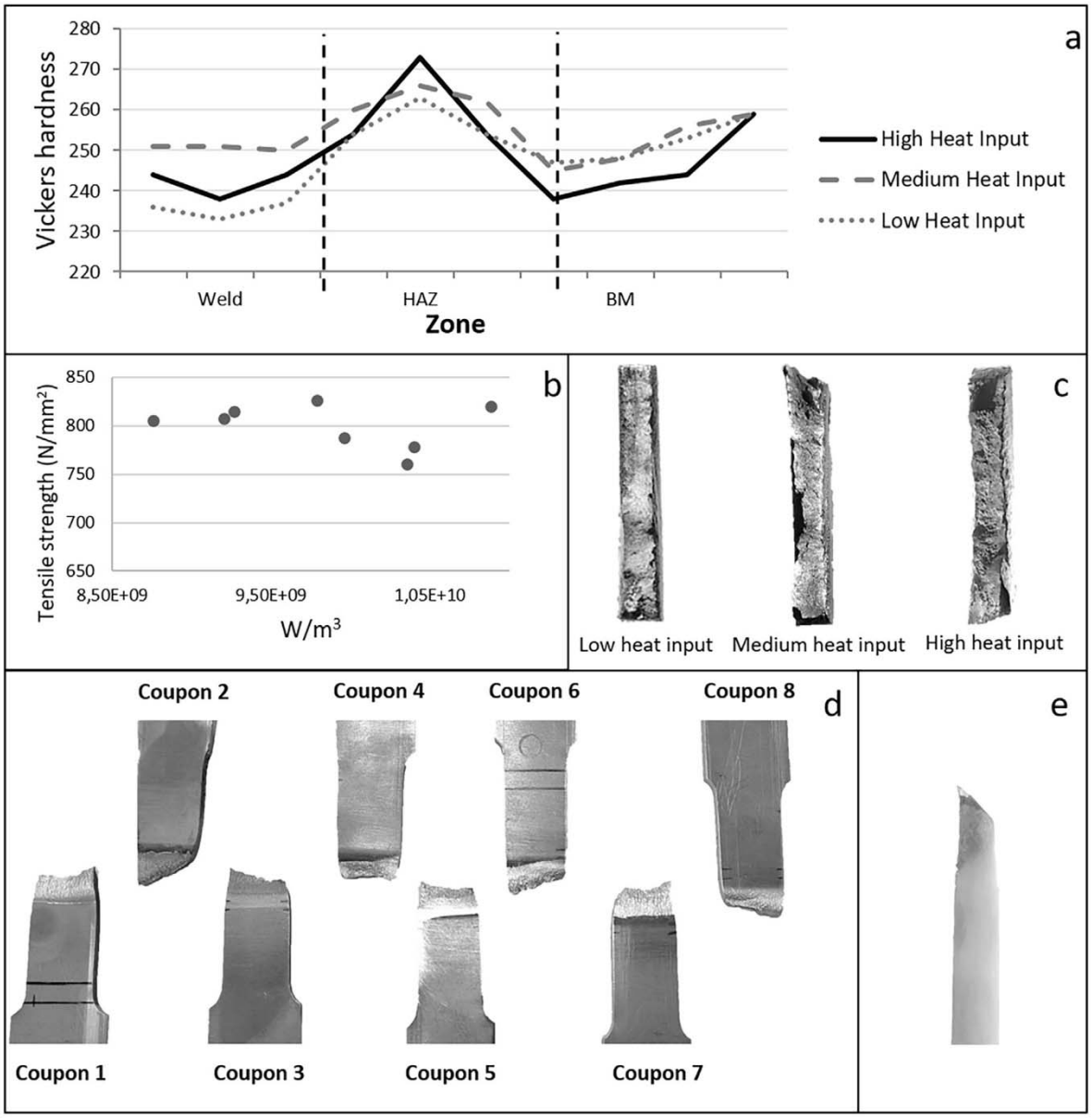

Fig. 7. (a) Vickers hardness versus heat input in the weld bead, the HAZ and the BM. (b) Tensile strength versus power transfer per volume (W/m^3). (c) Fracture surface of the tensile samples corresponding to low, medium and high heat input. (d) Plastic deformation in the eight samples corresponding to the weld coupons. (e) Fracture surface (bevel shaped).

the amount of ferrite obtained in each of the welding zones as a function of the heat input. The ferrite content is higher in the HAZ due to a faster cooling rate in this zone (Fig. 5d). The lines in Fig. 5a, b and 5d show the trends of the represented values.

Fig. 6 shows the influence of the main parameters – the geometry of the weld bead section, the maximum temperature reached and the cooling rate – on the proportion of ferrite in the weld bead. These parameters are expressed as power transfer per volume (W/m^3) [19]. Fig. 6a shows the influence of this parameter on the proportion of ferrite obtained. A low value implies less ferrite in the bead because there is less nitrogen loss, favouring the formation of austenite [41,42]. Fig. 6b shows the strong influence that the bead area has on the rate of cooling from the maximum temperature reached to 800 °C ($t_{max/8}$) in the zone. Because the geometry of the bead influences the heat flow, the cooling rate and the phase balance are modified.

The individual welding parameters that most influence power transfer per volume are the welding speed (Fig. 6c) and voltage (Fig. 6d). Increasing the welding speed results in a lower metal deposition rate, causing the bead area to be smaller and the cooling time to decrease. This increase in energy concentration results in a higher power transfer per volume. The influence of the voltage on power transfer per volume is due to the increase in energy and the modification of the geometry of the bead that it produces. Fig. 6c and d show that voltage exerts less of an influence than the welding speed. The change in the geometry of the joint, as previously mentioned, leads to a change in the heat distribution in the bead (Fig. 3e and f). The lines in Fig. 6a, b, 6c and d show the trends of the values represented.

Fig. 6e shows examples of the thermal cycling experienced by a line of nodes, from a starting temperature of 20 °C.

3.4. Vickers hardness and tensile testing

Fig. 7a shows the hardness measurements. The area of the weld bead presents greater variability in the results, as it depends on the composition of the filler metal, the dilution and the shielding gas. The composition of the filler metal is similar to that of the BM; therefore, the

microstructure of the molten metal without post-welding heat treatment justifies its lower hardness. The HAZ microstructure contains a high proportion of ferrite and a recrystallised microstructure, which justifies its higher hardness values. Fig. 7a shows that a lower heat input leads to a lower hardness. This is due to a faster cooling rate, which results in less time for austenite to form. The same phenomenon is also seen in the areas of the BM closest to the HAZ. In the BM zone, high hardness values are also observed as a consequence of a microstructure oriented by a deformation process, as observed in the micrograph in Fig. 4d. At the HAZ–BM interface (Fig. 7a), there is a small decrease in hardness compared with the BM. This is due to the fact that the thermal cycle in this zone of the BM restores the first phase of the recrystallisation treatments. This area is very small.

Fig. 7b shows the results obtained during the tensile tests. In all cases, the samples broke in a ductile manner in the area of the bead, as shown by the plastic deformation observed (Fig. 7d), the fibrous texture on the fracture surface (Fig. 7c) and the shape of the bevel fracture (Fig. 7e). This result makes sense because the bead is the weakest area, as shown by hardness tests. The relationship between the tensile strength reached and the power transfer per volume seems to indicate that increasing power transfer per volume promotes greater mechanical resistance. This is due to the fact that increasing the power transfer per volume promotes the formation of austenite, increasing the hardness and the tensile strength. All measured values are within the BM specifications (700–950 N/mm^2).

4. Conclusions

Several different parameters have been studied to analyse the effect of GMAW on UNS S32205, a DSS, including the hardness of the different areas of the weld, the microstructure, the dimensions of the weld bead, the thermal input and the phase balance. Finite element modelling served to complement the information on the thermal cycle that the piece undergoes, making it possible to determine how each parameter influences the different areas of the weld. From this work, the following conclusions have been made:

- The welding procedure used determines the nature of the obtained microstructure.
- At the microstructural level, in the area of the bead and in the HAZ, austenite is obtained in the form of needles (WA), AA and IA. The number of needles found in the HAZ is much lower the number found in the bead. In the HAZ, the cellular morphology shows austenite surrounding the ferrite grains, hindering the propagation of cracks.
- In the weld bead, the phase balance is directly related to the power transfer per unit volume (W/m^3). This parameter is more relevant than the energy provided per unit length (W/m^2), which is used to qualify procedures.
- The geometry of the bead influences the distribution of the heat flow towards the BM and, consequently, influences the thermal cycling and the phase balance.
- In the geometry of the bead, in addition to the heat input (which includes the influence of the parameters together), the influence of each parameter (voltage, current and the welding speed) must be considered individually.
- In the HAZ, the parameter that most influences the phase relationship is the cooling rate, determined by $t_{12/8}$.
- $t_{12/8}$ is defined by heat input and the geometry of the bead. An increase in $t_{12/8}$ favours the formation of austenite and a more equalised phase balance.
- To obtain the best phase balance, it is best to obtain a high $t_{12/8}$ and a small excess weld metal. This may be achieved by using high welding speeds and currents and low arc voltages.
- With this filler metal, the area of the weld bead is the least resistant, so its value is conditioned by the percentage of ferrite (the higher the percentage of austenite, the higher the resistance) and the power transfer per volume (the higher this value, the higher the tensile strength).

Funding

This research did not receive any specific grant from funding agencies in the public, commercial, or not-for-profit sectors.

Declaration of competing interest

The authors declare that they have no known competing financial interests or personal relationships that could have appeared to influence the work reported in this paper.

References

[1] R.N. Gunn, Duplex Stainless Steel, Abington Publishing, 1997.
[2] G.D. Caprio, Los Aceros Inoxidables, 1999. Grupinox.
[3] M. Aracil, Soldadura y corte de los Aceros Inoxidables, Cedinox, Asociación para la investigación y Desarrollo del Acero, 2018.
[4] IMOA, Directrices y prácticas para la fabricación de los Aceros Inóxidables Dúplex, 2012. United Kingdom.
[5] Cedinox. [Online]. Available: https://www.cedinox.es/opencms901/export/sites/cedinox/.galleries/fichas-tecnicastipos-espaol/ACX900-14462-2205.pdf. [accessed: Apr. 15, 2020].
[6] Corrosion problems in the chemical industry. Anti-corros, Meth. Mater. 11 (1964) 17–20.
[7] ASM International, Corrosion in the Petrochemical Industry, second ed., 2015.
[8] ASM International, ASM Handbook Volume 13C. Corrosion: Environments and Industries, 2006.
[9] A.A. Blanco, I. Gaspar, C. Negro, J. Tijero, B. López y, A. Álvarez-Barrientos, Rev. Metal. (Madr.) 1 (1998) 62–66.
[10] E. Korkmaz, C. Meran, Eng. Sci. Technol. 1 (2021) 503–513.
[11] S. Kumar, S.K. Nath, Int. J. Chem. Mol. Nucl. Mater. Metallurg. Eng. 8 (2014) 1056–1059.
[12] P.K. Ghosh, Introduction to gas metal arc welding process, in: Pulse Current Gas Metal Arc Welding, Springer, 2017.
[13] American Society for Metals, ASM Metals Handbook, vol. 6, Welding Brazing and Soldering, American Society for Metals, 1994.
[14] American Welding Society, Welding Handbook, ninth ed., 4, American Welding Society, 2011.
[15] G.S. da Fonseca, L.O.R. Barbosa, E.A. Ferreira, C.R. Xavier, J.A. de Castro, Metals 7 (2017) 538–559.
[16] G.H. Riesgo, Manual del Soldador, eleventh ed., Cesol, 2003.
[17] P.K. Ghosh, Pulse Current Gas Metal Arc: Characteristics, Control and Applications, Springer, 2017.
[18] R. Singh, Applied Welding Engineering: Processes, Codes, and Standards, Elsevier, 2020.
[19] Welding Handbook Committee, Welding Handbook, ninth ed., vol. 1, American Welding Society, 2011.
[20] Comité Técnico AEN/CTN 14 Soldadura y técnicas conexas. UNE-EN 1011-1:2010. "Recomendaciones para el soldeo de materiales metálicos. Parte 1: Guía general para soldeo por arco, 2010. Cesol.
[21] Abaqus, Keywords Reference Manual, vol. I, Abaqus, 2004. A–H (Version 6.5.
[22] P. van Erk IWE. Metrode Products Ltd. Lincoln Electric. Effective Welding of Duplex & Super Duplex Stainless Steel. United Kingdom.
[23] Comité técnico CTN 14 Soldadura y técnicas conexas, UNE-EN ISO 15614-1:2018 "Especificación y cualificación de los procedimientos de soldeo para los materiales metálicos, 2018. Cesol.
[24] ASM Handbook, Metallography and Microstructures (Volume vol. 9), ninth ed., ASM International, 2004.
[25] G. Vander Voort. Color Metallography. [Online]. Available: https://www.georgevandervoort.com/color-metallography/. (accessed: Mar 23 2020).
[26] Perfect Image, Clara Vision.
[27] CTN 36 Siderurgia, UNE-EN ISO 643:2020. Aceros, Determinación micrográfica del tamaño de grano aparente, 2020.
[28] Grani, Clara Vision.
[29] Comité técnico AEN/CTN 14 Soldadura y técnicas conexas, UNE-EN ISO 5817, Uniones soldadas por fusión en acero, níquel, titanio y sus aleaciones (excluido el soldeo por haz de electrones) Niveles de calidad para las imperfecciones, 2014. Cesol. 2014.
[30] Comité técnico CTN 7 Ensayos de Materiales, UNE-EN ISO 6507-1:2018. Materiales metálicos. Ensayo de dureza Vickers, Parte 1 Método de ensayo, 2018. Cesol.
[31] Comité Técnico CTN 7 Ensayos de materiales, UNE-EN ISO 6892-1:2017. Materiales metálicos. Ensayo de tracción. Parte 1: Método de ensayo a temperatura ambiente, 2017. Cesol.
[32] Abaqus, Simulia.
[33] G. Romaní, A. Portolés, Modelo tridimensional de simulación por MEF para estudiar la influencia de variables esenciales de soldadura robotizada GMAW en uniones a tope planas, Conference Book EUROJOIN6, 2006.

[34] J.L. Meseguer, A. Portolés, E.J. Martínez-Conesa, Int. J. Adv. Manuf. Technol. 98 (2018) 2449–2460.
[35] J.L.M. Valdenebro, E.J. Martínez-Conesa, A. Portolés, Therm. Sci. 23 (2019) 3639–3650.
[36] R.H.A. Abas, N.K. Taieh, Al-Khwarizmi, Eng. J. 11 (2015) 51–61.
[37] Make It From. [Online]. Available at: https://www.makeitfrom.com/(accessed: Jan. 15, 2021).
[38] Y. Dong, J.K. Hong, C.L. Tsai, P. Dong, Weld. J.. 76 (1997) 442–449.
[39] P. Dong, J. Zhang, M. Li, Mater. Sci. (1998).
[40] J.B.M. Vega. Alfa de Cronbach - Psicometría con R. 4, 4 (2018). [Online]. Available: https://medium.com/@jboscomendoza/alfa-de-cronbach-psicometr%C3%ADa-con-r55d3154806cf (accessed: Jan. 3, 2021)..
[41] V. Muthupandi, P. Bala Srinivasan, S.K. Seshadri, S. Sundaresan, Mater. Sci. Eng., A 358 (2003) 9–16.
[42] B. Varbai, T. Pickle, K. Májlinger, Int. J. Pres. Ves. Pip. 176 (2019).